Tunneling-to-hopping Transition in Multiheme Cytochrome Bioelectronic Junctions

Journal:	*The Journal of Physical Chemistry Letters*
Manuscript ID	jz-2022-03361v.R1
Manuscript Type:	Letter
Date Submitted by the Author:	n/a
Complete List of Authors:	Futera, Zdenek; University of South Bohemia, Faculty of Science Wu, Xiaojing; University College London, Department of Physics and Astronomy Blumberger, Jochen; University College London, Physics and Astronomy

Tunneling–to–hopping Transition in Multiheme Cytochrome Bioelectronic Junctions

Zdenek Futera,*,† Xiaojing Wu,‡ and Jochen Blumberger*,‡

†*Faculty of Science, University of South Bohemia, Branisovska 1760, 370 05 Ceske Budejovice, Czech Republic.*

‡*University College London, Department of Physics and Astronomy, Gower Street, London WC1E 6BT, UK.*

E-mail: z.futera@prf.jcu.cz; j.blumberger@ucl.ac.uk

Phone: +420 389 036 260 (ZF); ++44 (0)20-7679-4373 (JB)

Abstract

Multiheme cytochromes (MHCs) have attracted much interest for use in nanobioelectronic junctions due to their high electronic conductances. Recent measurements on dry MHC junctions suggested that a coherent tunneling mechanism is operative over surprisingly long distances, which challenges our understanding of coherent transport phenomena. Here we show that this is due to a rather low exponential decay constant in MHCs ($\beta = 0.2$ Å^{-1}) and exceptional robustness of the tunneling current against unfavorable energy-level offsets at the protein-electrode interface. Aligning the protein valance band with the Fermi level of the electrode, the transport mechanism changes from coherent tunneling to incoherent hopping at a protein size of about 7 nm, followed by a very shallow distance decay of the hopping current. Energy level alignment, which may be tuned by electrode modification or by applying a gate potential, thus plays a crucial role in governing the mechanism and efficiency of electron transport.

TOC Graphic

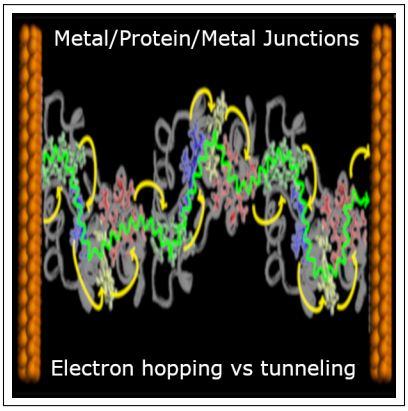

Molecular nanobiotechnology is a rapidly growing research field utilizing molecules and even whole proteins to manufacture accurate biosensors, efficient fuel cells, or biocatalysts. These applications exploit natural biocompatibility, high selectivity, and enzymatic activity of suitable proteins. Efficient mediation of electron flow across the protein and between the protein and metallic contacts is essential.[1–4] Therefore, redox-active metalloproteins known to mediate electron transfer in vivo, such as blue copper proteins and especially cytochromes, are good candidates for such applications.[5–10]

Multi-heme cytochromes belong to proteins that are naturally designed to transfer electrons over long distances, from nano to micrometers.[11] Structures of these proteins, resolved by the X-ray diffraction techniques, revealed a unique arrangement of the heme cofactors into linear and/or branched chains.[12–16] The cofactors are covalently bound to the protein matrix and contain bis-histidine coordinated Fe-hemes in a low-spin state, which is responsible for the redox activity of these proteins. It was shown by computational techniques[17–21] and later confirmed experimentally,[22–24] that under natural conditions (aqueous solution, electron transfer initiated by a molecular electron donor, not an electrode) electron transfer across the protein occurs via incoherent hopping between nearest neighbour heme cofactors.[11,25] Computations have predicted heme-to-heme ET rates up to $\sim 10^9$ s^{-1} in these proteins,[20,26] which was subsequently confirmed by pump-probe transient absorption spectroscopy,[23,24] and a intrinsic (i.e. protein-limited) electron hopping flux across the protein of $\sim 10^5$ s^{-1} for the decaheme cytochromes MtrC, MtrF[26] and MtrAB[21] and $\sim 10^6$ s^{-1} for the tetraheme cytochrome STC.[20]

In nanobioelectronic applications the natural molecular electron donor and acceptor are replaced by two metal electrodes and the protein may no longer be fully hydrated but exposed to air or even vacuum. The transport process under these non-native conditions may be different from the hopping scenario described above.[27] Indeed when protein monolayers of small tetra-heme cytochrome (STC), or deca-heme cytochrome MtrF were probed by the suspended nanowire technique in vacuum, temperature-independent currents were detected,

in contrast with predictions of thermally-activated hopping models. Therefore, coherent tunneling was suggested as the electron transport mechanism in these junctions. However, the high magnitudes of the measured currents are rather exceptional, pointing to the potentially unusual electronic properties of multi-heme cytochromes. For example, tunneling currents in STC junctions were observed to be three orders of magnitude greater than in Azurin, which is a blue-copper protein of a similar size as STC.[10]

To obtain further mechanistic insight, it would be desirable to study charge transport in MHC junctions by direct charge propagation using non-adiabatic molecular dynamics techniques,[28] or analyzed by sophisticated models capturing, for example, quantum interference effects, charge carrier generation and recombination, or their incoherent scattering on defects and lattice vibrations.[29,30] However, these methods are typically very computationally demanding and currently not applicable on the extended heterogeneous bio/metallic interfaces like protein junctions. Recently, we have established a computational protocol for coherent tunneling current calculation in protein junctions based on the Landauer-Büttiker formalism in combination with DFT+Σ method.[31] Application of this methodology to Au-STC-Au junctions provided I-V curves in excellent agreement with the measurements by Cahen and co-workers[10] giving further support to the view that transport in these junction occurs via coherent tunneling. Our DFT+Σ calculations showed that the currents are facilitated by a large number of valence-band states of the STC protein due to a significant offset ($\sim$1.2 eV) between the protein states and the electrode Fermi level resulting in an off-resonant tunneling regime. Interestingly, the contribution of Fe-states to the current was found to be minor, which is in stark contrast to electron hopping in solutions where the charge is localized on the iron centers and first shell ligands.[32,33]

In this work we investigate one fundamental question: given that transport occurs by coherent tunneling in small multi-heme protein junctions, how is it possible then that larger multi-heme proteins and their complexes and wires conduct electrons over 100 nm – 1 μm-long junctions in experiment.[15,34] On this length scale any coherent transport must have fully

decayed. Our hypothesis is that there must be a critical distance where the exponentially decaying coherent tunneling crosses over into hopping. The latter has a more shallow polynomial decay and is expected to support transport over far greater distances than coherent tunneling. In fact, such cross-over was experimentally observed for hole-transfer along stacks of DNA base pairs[35] and, more recently and relevant to the current study, in junctions made of π-conjugated oligomers.[36] Does such a cross-over also occur in multi-heme junctions? If so, at which protein length/electrode separation? And how do other parameters such as the alignment between protein electronic states and electrode Fermi level, or the density of states affect this crossover?

To answer these fundamental questions, we present herein large-scale, all-QM DFT-level conductance calculations for dry STC junction models in different protein orientations, and combine them with experimental conductance data[10] for dry protein monolayer junctions to predict the exponential distance decay of the tunneling current for these proteins. We also calculate the heme-to-heme hopping current for these junctions and their distance dependence. Remarkably, we find that under the experimental conditions hopping is not competitive with tunneling because of the large mismatch between the top of the protein valence band (highest occupied molecular orbital, HOMO) and the Fermi level of the electrodes used in experiment (1.2 eV). This results in very small metal-to-heme electron hole injection rate constants, whilst the effect of the energetic mismatch on the tunneling current is much smaller in comparison. If this energy mismatch is removed (e.g. by application of a gate voltage or use of different electrode materials with better energy level alignment), hopping transport is predicted to dominate over tunneling for distances exceeding $\sim$7 nm.

Atomistic models of gold STC junctions were prepared for conditions similar to those used in the experimental measurements of Cahen and co-workers (vacuum at 10^{-5} bar).[10] In the previous work[31] we used the S87C mutant of the X-ray crystal structure of STC (taken from the PDB database, code 1M1Q[12]), relaxed it in vacuum where all solvent water molecules were removed and three structural water molecules within the protein were retained, and

adsorbed on the flat gold (111) surface using the polarizable GolP-CHARMM force field.[37–39] We generated 144 adsorption structures of STC on Au(111) and found that they can be generally classified as "lying" or "standing" configurations.[31] In this work, we select the two energetically most favorable of each of the two motifs, further referred as **L1**, **L2**, **S1**, and **S2**, were selected for further MD simulations. Following the experimental setup, we chemically attach those 4 structures to the gold surface by Cys87 sulfur[10,31] and the second gold surface was added to form the junctions. The distance between the two gold slabs was then slowly shortened while monitoring the internal protein pressure[40,41] to optimize the junction widths (see SI for details). The obtained pressure curves are shown in Figure 1 together with the final geometries of the four STC junctions. While the "lying" junction widths (26.8 Å and 28.1 Å for **L1** and **L2**) are within the error bar of the experimental monolayer widths, 24 ± 5 Å (indicated by the blue regions in the Figure 1 plots), the two "standing" structures have considerably larger electrode separation distances (40.5 Å and 36.3 Å for **S1** and **S2**). The protein secondary structure elements are stable in all four STC configurations except an α-helix which is in contact with electrode.

Considering the heme-cofactor arrangement in the STC junctions, the "standing" structures **S1** and **S2** form connections resembling the molecular wires where the protein is in contact with each electrode surface by one heme only. However, as can be seen from the corresponding pressure profiles with varying distance (Figure 1c and 1d), these structures are metastable and may, on a time scale much longer than the current MD simulations, further relax into the energetically most favorable "lying" configuration, especially at higher external pressures. In the **L1** and **L2** structures, STC is firmly inserted between the two electrodes. The orientation is such that the two terminal hemes 1 and 4 are in close proximity with one electrode and hemes 2 and 3, located in the middle of the protein, are in close proximity with the other electrode. Such configuration suggests a bifurcated electronic charge transport through the protein, as we explored in detail in our recent study of the **L1** junction.[31] Nevertheless, the heme 4 near the C-terminus in **L2** is relatively far from the surface (heme

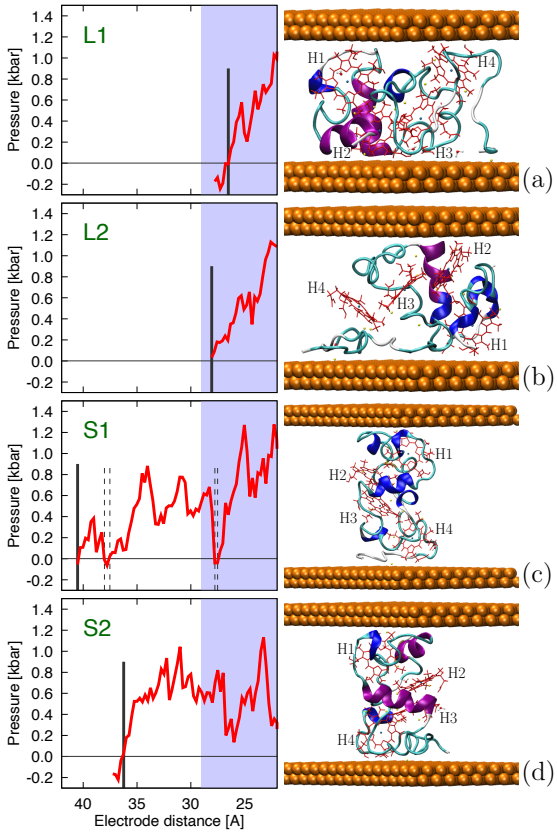

Figure 1: Structures of Au-STC-Au junctions. Calculated profile of the internal protein pressure as a function of electrode separation distance (left) and atomistic structures of the junctions (right) with heme cofactors highlighted in red color and gold atoms represented as orange spheres. The electrode–electrode separation distance, marked in the graphs by vertical thick black lines, are (a) 26.8 Å and (b) 28.1 Å for the two lying structures **L1** and **L2** and (c) 40.5 Å and (d) 36.3 Å for the two standing structures **S1** and **S2**. Dashed vertical lines in the graphs mark distances with the internal protein pressure close to zero while the blue regions indicate experimental STC monolayer width.[10]

edge to gold distance 9.4 Å compared to 4.4 Å in **L1**) and the C-terminal α-helix, which is unfolded in the dry STC structures, is fully adsorbed to the surface in contrast to the **L1** structure where it forms a link between the two electrodes (compare Figure 1a and 1b).

Next, we calculated the tunneling current from the DFT electronic structure data for STC in the all-reduced state. We use the Landauer-Büttiker formalism where the current is obtained by integrating the transmission function over the Fermi window at a given bias

potential,

$$I(V) = \frac{e}{\pi\hbar} \int T(E) \left[f_L(E,V) - f_R(E,V) \right] dE. \tag{1}$$

The Fermi-Dirac distributions f_M, $M = \{L, R\}$ on the left (L) and right (R) electrodes, respectively, determine the state occupation for the tunneling energy E and the bias potential V. The transmission function was obtained in the Breit-Wigner approximation of independent conduction channels

$$T(E) = \sum_{j \in \text{protein}} \frac{\Gamma_j^{(L)}(E)\Gamma_j^{(R)}(E)}{[E - \epsilon_{\Sigma_j}]^2 + [\Gamma_j^{(L)}(E) + \Gamma_j^{(R)}(E)]^2/4} \tag{2}$$

The spectral density functions $\Gamma_j^{(M)}$ of molecular states j are computed from the electronic coupling elements $[H_{MP}]_{mj}$ between the protein (P) states j and the electrode (M) states m, and weighted by the metallic density of states ρ_M,

$$\Gamma_j^{(M)}(E) = 2\pi \left[|[H_{MP}]_{mj}|^2 \rho_M(\epsilon_{M,m}) \right]_{\epsilon_{M,m}=E} \tag{3}$$

The electronic structure of the protein junctions were computed at the DFT level of theory using the PBE functional,[42] the DZVP basis set and GTH pseudopotentials,[43] as implemented in the CP2K software package.[44] The Kohn–Sham states were localized on the protein and the left and right electrodes using the projector operator based diabatization (POD) approach.[31,45] The band alignment of protein electronic states with respect to the electrode Fermi level was corrected using the DFT+Σ approach[46,47] resulting in protein-corrected energy levels ϵ_{Σ_j}. After correction, the top of the protein valence band of the oxidized protein was at 1.2 eV below the Fermi level E_f of the gold, in good agreement with ultraviolet photoelectron spectroscopy (UPS) measurements.[31] The same occupied-state shift was applied to all the reduced junctions while the computed unoccupied-state corrections were used. Electronic coupling matrix elements between the protein and metallic states, $[H_{MP}]_{mj}$, are contained in the off-diagonal block obtained after POD diabatization and are

used to construct the spectral density functions (Equation 3) needed for the transport calculations. POD electronic couplings were shown to give similar results as other diabatization schemes, e.g., CDFT.[48,49] Further details of the calculations are given in the SI.

The computed currents are shown in Figure 2 together with the transmission function in the Fermi window energy region. In experimental UPS measurements the top of the valence band of STC was shown to be 1.2 eV below the Fermi level of the electrode,[31] in a good agreement with our DFT+Σ calculations. In this off-resonant tunneling regime, the transmission function is practically flat in the Fermi window and the corresponding current-voltage (I-V) curves are linear within the $\pm$0.5 V range of the applied bias potential, for all four structures. The current magnitude decays with the junction width, dropping from 18.5 nA at 0.5 V for the "lying" structure **L1** of width 26.8 Å to 1.5 nA for the "standing" structure **S1** of width 40.5 Å. The computed distance dependence of tunneling current is plotted in Figure 3, where we also added experimental data for junctions of STC,[10] for MtrF[10,50] and MtrC[51] covering tunneling distances up to 5 nm. The combined computed and experimental data fit very well to a single exponential decay, $I \propto Ae^{-\beta r}$, with a decay constant $\beta = 0.20$ Å^{-1} ($R^2 = 0.99$). For the experimental data set only, $\beta = 0.22$ Å^{-1} ($R^2 = 0.99$), while for the computed data only we obtained slightly smaller $\beta = 0.17$ Å^{-1} ($R^2 = 0.95$).

The offset of the protein valence band edge with respect to the Fermi level (E_f) depends, of course, on the electrode material, its crystallinity, the exposed surface facet, the degree of oxidation or passivation, among many other factors. Moreover, in certain experimental setups, e.g. electrochemical STM, the offset can be controlled by application of a gate potential. Hence, it is of interest to understand how the I-V response changes upon moving the protein valence band edge closer to the electrode Fermi level. In this case the heme levels come close to or insert between the Fermi levels of the electrodes, a situation that can lead to charging of the protein and/or a change in the transport mechanism. Moreover, the Kohn-Sham DFT based on the single-determinant representation of the wavefunction

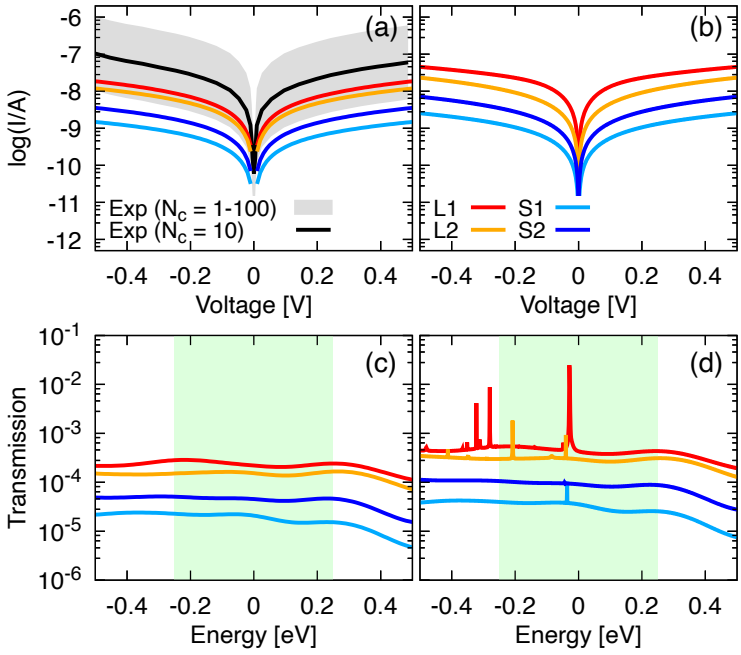

Figure 2: Calculated I-V curves for the **L1**, **L2**, **S1** and **S2** junction structures in (a) off-resonant tunneling regime with band alignment estimated by DFT+Σ and in (b) hypothetical resonant regime where the protein valenced-band edge is aligned with the electrode Fermi energy. Corresponding transmission functions for both tunneling regimes are shown in panels (c) and (d), respectively. The Fermi window corresponding to bias potential $\pm$0.5 V is shown in green. The experimental I-V curve (black) is obtained from the data reported in Ref. 10. Assuming 10 STC protein contacts per junction, the measured current was divided by factor 10. The area shown in grey represents the corresponding uncertainty, 1–100 protein contacts.

may no longer be appropriate for the resonant cases, where a multi-reference description may be required.[52] However, such methods are computationally demanding and impractical for systems as large as protein junctions. With these caveats in mind we calculate here the coherent tunneling current for the resonant case where the protein HOMO, representing the valence band maximum of the fully-reduced STC, is aligned with E_f. The obtained I-V curves and the corresponding transmission functions are shown in Figure 2b and 2d, respectively.

Now, the transmission function exhibits a series of peaks (Figure 2d for **L1**) – the largest peak has a peak height $\sim$0.03 and is located 0.03 eV below the Fermi level. This peak corresponds to iron t_{2g} states which become the dominant conduction channels in this regime.

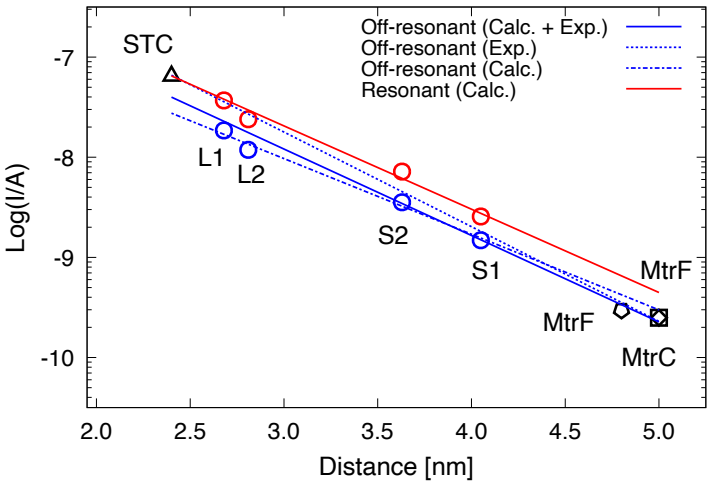

Figure 3: Distance decay of coherent tunneling currents in MHC junctions. The joint set of calculated log currents (STC in **L1**, **L2**, **S1** and **S2** orientation, Equation 1–3, circles) and experimental log currents (STC, triangle[10] – measured current divided by 10 assuming 10 protein contacts per junction; MtrF, pentagon[10] – measured current divided by 5 assuming 5 protein contact per junction; MtrF, square[50] – single protein measurements; MtrC, diamond[51] – single protein STM) at 0.5 V bias are fit to linear regressions (solid blue). Fits to calculated data only (blue dashed) and experimental data only (blue dotted) are also shown. Corresponding exponential decay coefficients β (defined by $I \propto e^{-\beta r}$) are summarized in Table S2 in the SI. Data for hypothetical resonant tunneling is shown in red (calculation only).

The resulting I-V curve exhibits rapid increase in a low potential region. The peaks down to about -0.3 eV also originate from iron states of the heme cofactors, however, their energies are beyond the considered Fermi window and they don't affect the current curve in the $\pm$0.5 V potential range. The structure **L2**, although it has a similar size as the structure **L1**, is less favorably adsorbed to the gold electrodes preventing larger effects of the iron states on the conductance because of their small coupling with the electrode states. Only one narrow peak at 0.2 eV below E_f is observed which does not affect the smooth shape of the I-V curve. In the wider **S1** and **S2** junctions, the iron states do not practically contribute to the conduction channels at all. Overall, the current decay with STC-junction width is similar both in the resonant and off-resonant tunneling regime ($\beta = 0.19$ Å^{-1} and 0.17 Å^{-1}, respectively).

In the coherent tunneling mechanism that is characteristic for single protein STC junc-

tions, the tunneling electrons transiently occupy delocalized protein states (termed conductions channels) that connect the two electrodes. For an illustration of the conduction channels that contribute most to the current in the STC **L1** orientation, we refer to Ref. 31 (Figure S9). However, considering junctions made of larger proteins or stacked protein complexes the efficiency of the coherent transport decays exponentially. For instance, adopting the exponential decay constant from above, $\beta = 0.20$ Å^{-1}, and assuming a typical voltage of 0.5 V, the current is predicted to become vanishingly small, $< 10^{-14}$ A for distances > 10 nm. Yet, the multi-heme cytochromes are known to transfer electrons over micrometer-long distances when they are suitably packed,[5,7,15,34,53,54] suggesting that at a certain critical distance coherent tunneling crosses over to incoherent heme-to-heme hopping.

As recent transport measurements on MtrF were interpreted in terms of coherent tunneling models, the critical crossover distance can be expected to be in excess of the size of this protein, > 5 nm. Thus we consider junctions made of multiple STC proteins, where one STC is stacked on top of another, see Figure 4a, and calculate the incoherent current due to sequential heme-to-heme hopping as a function of the number of STC repeat units in the junction. The optimized **S2** structure of STC is used as a basic protein repeat unit. The structure of the STC stack is modelled to reproduce the ABAB... stacking pattern and the inter-protein heme-to-heme distances found in the X-ray structure of STC protein crystals.[54] Heme 1 is coupled to the right (R) electrode and heme 4 to the left (L) electrode as indicated in Figure S8 in SI. The states $i = 2, 3$ do not interact directly with the R, L electrodes, however, they exchange electrons with their nearest heme neighbours. The rate equation for the electron population of heme 1, P_1, is then

$$\frac{dP_1}{dt} = (k_{1L} + k_{12}P_2)(1 - P_1) - (k_{L1} + k_{21}(1 - P_2))P_1 \tag{4}$$

and similarly for the other hemes. The resulting set of coupled rate equations (i.e., classical Master equation) is solved iteratively to obtain the steady state flux and the current across

the junction, as explained in detail in the SI.

The heme-to-heme electron transfer rate constant were calculated using the non-adiabatic Marcus formula,

$$k_{ij} = \frac{2\pi}{\hbar} \left\langle |H_{ij}|^2 \right\rangle \frac{1}{\sqrt{4\pi\lambda_{ij} k_B T}} \exp\left(-\frac{(\lambda_{ij} + \Delta G_{ij})^2}{4\lambda_{ij} k_B T} \right) \tag{5}$$

where H_{ij} are electronic coupling elements obtained from POD calculation, λ_{ij} are the reorganization free energies for heme-to-heme ET in vacuum, obtained by MD simulations, and the ET free energy difference or driving forces, $\Delta G_{ij} = e(\epsilon_j - \epsilon_i)$ are obtained as the difference of experimentally determined heme reduction potentials while taking into account the potential drop due to the bias voltage. Positions of the heme-cofactor reduction potentials in vacuum STC structure on the gold interface were estimated from the electronic band alignment obtained by DFT calculations. The interfacial electron transfer rates from metal to heme i, k_{iM} ($i = 1$ or 4), are calculated using the Marcus–Hush–Chidsey expression,

$$k_{iM} = \frac{\Gamma}{\hbar} \sqrt{\frac{k_B T}{4\pi\lambda_i}} \int_{-\infty}^{\infty} \exp\left[-\left(x - \frac{\lambda_i + e(\mu_M - \epsilon_i)}{k_B T} \right)^2 \frac{k_B T}{4\lambda_i} \right] / \left[1 + \exp(x) \right] dx \tag{6}$$

For the reverse direction, k_{Mi}, the same expression is used with the sign of the term $e(\mu_M - \epsilon_i)$ multiplied with -1. The interfacial electronic couplings are between the HOMO of the Fe^{2+} heme i (1 or 4) and the metal electronic state. In the above equation we considered the couplings to be energy independent (i.e., wide band approximation) and take an average value suitably weighted with the density of electronic states, ρ

$$\Gamma = 2\pi \left\langle |H_{iM}|^2 \rho \right\rangle \tag{7}$$

Specific details of the calculation of all ET parameters can be found in SI.

The computed distance dependencies of the incoherent hopping and coherent tunneling currents are shown in Figure 4b (blue lines). For the single STC junction (structure **S2**,

3.6 nm) the hopping current (dashed blue) is more than 10 orders of magnitude smaller than the coherent tunneling current (solid blue) showing that the hopping can be safely ruled out, in accord with the experimental observation that the current is close to temperature-independent. The hopping current is strongly limited by the very slow electron transfer from the heme redox cofactor 1 to the metal electrode, with a rate constant of 33.8 s^{-1} (that is, orders of magnitude smaller than the micro to nanosecond rates for heme-to-heme ET in STC). The reason for this is the major energy level mismatch between the Fe^{2+}/Fe^{3+} redox levels of the hemes and the Fermi level of the electrodes, about 0.8 eV at zero voltage (see Figure S8a in SI obtained from the energy level offset from photoemission measurements, 1.2 eV, minus the computed reorganization free energy for heme oxidation in vacuum, 0.4 eV, see SI for details), resulting in a very small Franck-Condon factor for heterogeneous ET (integral over density over states in Equation 6). Hopping conduction starts to become competitive with coherent tunneling only at extremely long distances ($>$ 20 nm) corresponding to chains made of 6 STC proteins. However, this crossover cannot be observed because the current magnitudes at this point are vanishingly small and cannot be detected.

The mismatch between protein redox levels and the electrode Fermi levels could be reduced in many ways, e.g. facet engineering, surface modifications, use of different electrode materials with different work functions or the application of a gate potential, as often utilized in nanoelectronic devices. Therefore, we model also the limiting case where heme 1 is aligned with the gold-electrode Fermi level under zero-bias conditions. The heme redox levels for this condition and at a bias potential of 0.5 V is illustrated in Figure S8b in SI. For the single STC junction (**S2** structure, 3.6 nm) the hopping current ($\sim 10^{-10}$ A, red dashed line) is now much closer to, though still appreciably smaller than the coherent tunneling current ($\sim 10^{-8}$ A, red solid line).

Yet, for stacks of 2 STC proteins ($\sim$7 nm) the hopping current is about as large as the tunneling current. For longer stacks, hopping rapidly becomes the dominant transport mechanism owing to the shallower distance decay ($\propto 1/r^{0.98}$, $R^2 = 0.95$). Extrapolating the

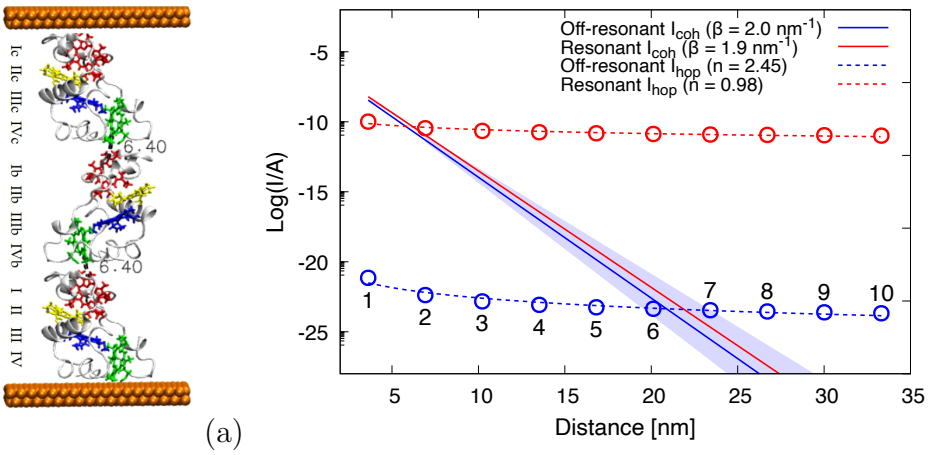

Figure 4: (a) Model of Gold-$(STC)_3$-Gold junction based on the **S2** single protein junction with STC–STC protein alignment taken from the STC protein crystal structure.[54] Hemes I, II, III, and IV are highlighted in red, yellow, blue, and green, respectively. (b) Predicted distance decay of electronic currents through stacked STC junctions. The computed hopping currents I_{hop} are shown in circles, with specified number of the stacked STC units, and fit to a polynomial decay, $I_{\text{hop}} \propto r^{-n}$ (dashed lines). Coherent tunneling currents, $I_{\text{coh}} \propto e^{-\beta r}$, (solid lines) are taken from Figure 3. Data for the off-resonant regime (protein valence band maximum located 1.2 eV below E_f) are shown in blue and data for the hypothetical resonant regime (protein valence band maximum aligned with E_f) in red. In shaded blue the range of exponential decay obtained using computed or experimental data only. Notice the crossover from coherent tunneling to hopping in the resonant regime at about 7 nm.

fit to even longer distances, we predict that pA currents are sustainable up to ~ 0.3 μm and 0.3 pA at 1 μm, assuming idealized STC stacks as the one shown in Figure S8 in SI. Hence, our calculations predict that the level alignment not only affects the efficiency of the charge transport but also the transport mechanism for conduction.

Interestingly, the shallow exponential distance decay determined here for MHCs ($\beta \approx 0.2$ Å^{-1}) is rather similar to the value determined recently by Frisbie and co-workers for junctions of π-conjugated organic oligomer wires ($\beta = 0.3$ Å^{-1}).[36] The small decay constant in MHCs despite significant energy level offset of 1.2 eV cannot be explained by simple tunneling models that treat the protein as a structureless insulator as, e.g., in the square barrier tunneling and Simmons models.[55] The latter, derived for tunnelling through insulating media of general barrier shapes, gives excellent fits to experimental (and computed) I-V data for

MHCs,[10] but the tunneling lengths obtained from these fits (12.2 Å for STC in **L1** orientation[31]) are unphysical – they are much shorter than the actual protein lengths (26.8 Å). On the other hand, the *I-V* curves from experiment and from multi-channel Landauer-Büttiker DFT+Σ calculations fit very well an effective single-channel Landauer model with physically meaningful values of 0.56 eV for an effective energy level offset of the conduction channel with respect to the Fermi level and an effective protein-electronic coupling of 6.2 meV (values again for STC in **L1** orientation from Ref. 31.)

A crossover from coherent tunneling to hopping as predicted here for MHCs has been reported before, e.g., in the junctions of organic oligomers mentioned above,[36] at oligomer lengths of 4 nm, and for DNA, after 3 base-pairs[35] (although in the latter example short to medium-range transport was later thought to occur via flickering resonance[56]). The larger crossover distance predicted here for MHCs, 7 nm, could be due to several reasons including the slightly lower exponential distance decay, the higher density of electronic states in proteins and, possibly, smaller hopping rates disfavouring hopping transport. In this respect, we note that the average density of protein states in the valence band of STC (84 eV^{-1}) is about a factor of 10 higher than in the oligomer wires studied by Frisbie (7 eV^{-1}).[36] If one evaluates the transmission function for STC for a modified density of states that corresponds to the one for the oligomer wire above (by taking into account only every 12th protein electronic state in the sum on the RHS of Eq.2), the coherent tunneling current drops by about an order of magnitude (while the effect on β is very small). This decreases the crossover distance from tunneling to hopping to a value that is very similar to the one observed for the oligomer wires. This implies that the high density of protein electronic states helps prolong the coherent tunneling regime to distances that exceed the ones in molecular wires made of small molecules.

In summary, we investigated conductive properties of multi-heme protein junctions between gold-electrode contacts by large-scale, state-of-the-art DFT calculations and explored the efficiency of the coherent tunneling and incoherent hopping electron transport mech-

anisms. Small-tetraheme cytochrome (STC) was used as a model system because of its relatively small size suitable for the electronic-structure calculations and available experimental electron transport data.[10,54] We have shown that the relatively large offset between protein valence band edge and Fermi energy of the gold electrodes (1.2 eV), together with strong protein adsorption and sizable protein-electrode electronic couplings, gives rise to a coherent off-resonant tunneling regime. Under these conditions, the hopping mechanism is uncompetitive due to the large potential drop at the interface and vanishingly small electron hole injection rates. These findings are in accord with the experimental observations of the temperature independent current-voltage response of the single-protein gold junctions that cannot be explained within the incoherent hopping models.[10,31] Importantly, we predict a crossover of transport mechanism from coherent tunneling to incoherent hopping for MHCs spanning junction widths > 7 nm, along with temperature-dependent currents, provided that charge injection and ejection rates at the electrodes are sufficiently fast. This near-resonant regime should be experimentally accessible by suitable modification of the electrode work function and/or by gating.

Acknowledgement

We would like to thank David Cahen (Weizmann Institute of Science) for insightful discussions. X.W. was supported by the European Research Council (ERC) under the European Union Horizon 2020 research and innovation program (Grant Agreement No. 682539/SOFTCHARGE). Z.F. was supported by the Czech Science Foundation (project 20-02067Y) and is grateful for computational resources supplied by the project "e-Infrastruktura CZ" (e-INFRA LM2018140) provided within the program Projects of Large Research, Development and Innovations Infrastructures. Via our membership of the UK's HEC Materials Chemistry Consortium, which is funded by EPSRC (Grant Nos. EP/L000202 and EP/R029431), this work used the ARCHER UK National Supercomputing Service as well as the UK Materi-

als and Molecular Modeling (MMM) Hub, which is partially funded by EPSRC (Grant No. EP/P020194), for computational resources.

Supporting Information Available

Simulation details and electronic structure calculations, parameters and the coherent tunneling and incoherent hopping electron-transport models, junction densities of states, structures and currents for the oxidized STC junctions, numerical values of the computed junction currents.

References

(1) Rinaldi, R.; Biasco, A.; Maruccio, G.; Cingolani, R.; Alliata, D.; Andolfi, L.; Facci, P.; De Rienzo, F.; Di Felice, R.; Molinari, E. Solid-State Molecular Rectifier Based on Self-Organized Metalloproteins. *Adv. Mater.* **2002**, *14*, 1453–1457.

(2) Amdursky, N.; Ferber, D.; Bortolotti, C. A.; Dolgikh, D. A.; Chertkova, R. V.; Pecht, I.; Sheves, M.; Cahen, D. Solid-State Electron Transport via Cytochrome c Depends on Electronic Coupling to Electrodes and Across the Protein. *Proc. Nat. Acad. Sci.* **2014**, *111*, 5556–5561.

(3) Zhang, A.; Lieber, C. M. Nano-Bioelecronics. *Chem. Rev.* **2016**, *116*, 215–257.

(4) Bostick, C. D.; Mukhopadhyay, S.; Pecht, I.; Sheves, M.; Cahen, D.; Lederman, D. Protein Bioelectronics: A Review of What We Do and Do Not Know. *Rep. Prog. Phys.* **2018**, *81*, 26601.

(5) Leung, K. M.; Wanger, G.; El-Naggar, M. Y.; Gorby, Y.; Southam, G.; Lau, W. M.; Yang, J. Shewanella oneidensis MR-1 Bacterial Nanowires Exhibit p-Type Tunable Electronic Behavior. *Nano Lett.* **2013**, *13*, 2407–2411.

(6) Amdursky, N.; Marchak, D.; Sepunaru, L.; Pecht, I.; Sheves, M.; Cahen, D. Electronic Transport via Proteins. *Adv. Mater.* **2014**, *26*, 7142–7161.

(7) Chong, G. W.; Karbelkar, A. A.; El-Naggar, M. Y. Nature's Conductors: What Can Microbial Multi-Heme Cytochromes Teach Us About Electron Transport and Biological Energy Conversion? *Curr. Opin. Chem. Biol.* **2018**, *47*, 7–17.

(8) Ing, N. L.; El-Naggar, M. Y.; Hochbaum, A. I. Going the Distance: Long-Range Conductivity in Protein and Peptide Bioelectronic Materials. *J. Phys. Chem. B* **2018**, *122*, 10403–10423.

(9) Kayser, B.; Fereiro, J. A.; Guo, C.; Cohen, S. R.; Sheves, M.; Pecht, I.; Cahen, D. Transistor Configuration Yields Energy Level Control in Protein-Based Junctions. *Nanoscale* **2018**, *10*, 21712–21720.

(10) Garg, K.; Ghosh, M.; Eliash, T.; van Wonderen, J. H.; Butt, J. N.; Shi, L.; Jian, X.; Futera, Z.; Blumberger, J.; Pecht, I. et al. Direct Evidence for Heme-Assisted Solid-State Electronic Conduction in Multi-Heme c-Type Cytochromes. *Chem. Sci.* **2018**, *9*, 7304–7310.

(11) Blumberger, J. Electron Transfer and Transport through Multi-Heme Proteins: Recent Progress and Future Directions. *Curr. Opin. Chem. Biol.* **2018**, *47*, 24–31.

(12) Leys, D.; Meyer, T. E.; Tsapin, A. S.; Nealson, K. H.; Cusanovich, M. A.; Van Beeumen, J. J. Crystal Structures at Atomic Resolution Reveal the Novel Concept of "Electron-Harvesting" as a Role for the Small Tetraheme Cytochrome c. *J. Biol. Chem.* **2002**, *277*, 35703–35711.

(13) Clarke, T. A.; Edwards, M. J.; Gates, A. J.; Hall, A.; White, G. F.; Bradley, J.; Reardon, C. L.; Shi, L.; Beliaev, A. S.; Marshall, M. J. et al. Structure of a Bacterial Cell Surface Decaheme Electron Conduit. *Proc. Nat. Acad. Sci.* **2011**, *108*, 9384–9389.

(14) Edwards, M. J.; White, G. F.; Norman, M.; Tome-Fernandez, A.; Ainsworth, E.; Shi, L.; Fredrickson, J. K.; Zachara, J. M.; Butt, J. N.; Richardson, D. J. et al. Extracellular Decaheme Proteins Involved in Microbe-Mineral Electron Transfer. *Sci. Rep.* **2015**, *5*, 11677.

(15) Wang, F.; Gu, Y.; O'Brien, J. P.; Yi, M. S.; Yalcin, S. E.; Srikanth, V.; Shen, C.; Vu, D.; Ing, N. L.; Hochbaum, A. I. et al. Structure of Microbial Nanowires Reveals Stacked Hemes that Transport Electrons over Micrometers. *Cell* **2019**, *177*, 361–369.

(16) Edwards, M. J.; White, G. F.; Butt, J. N.; Richardson, D. J.; Clarke, T. A. The Crystal

Structure of a Biological Insulated Transmembrane Molecular Wire. *Cell* **2020**, *181*, 1–9.

(17) Breuer, M.; Zarzycki, P.; Blumberger, J.; Rosso, K. M. Thermodynamics of Electron Flow in the Bacterial Deca-heme Cytochrome MtrF. *J. Am. Chem. Soc.* **2012**, *134*, 9868–9871.

(18) Breuer, M.; Zarzycki, P.; Clarke, T. A.; Edwards, M. J.; Butt, J. N.; Richardson, D. J.; Fredrickson, J. K.; Zachara, J. M.; Blumberger, J.; Rosso, K. M. Molecular Structure and Free Energy Landscape for Electron Transport in the Decahaem Cytochrome MtrF. *Biochem. Soc. Trans.* **2012**, *40*, 1198–1203.

(19) Breuer, M.; Rosso, K. M.; Blumberger, J. Electron Flow in Multiheme Bacterial Cytochromes is a Balancing Act Between Heme Electroonic Interaction and Redox Potentials. *Proc. Nat. Acad. Sci.* **2014**, *111*, 611–616.

(20) Jiang, X.; Futera, Z.; Ali, M. E.; Gajdos, F.; von Rudorff, G. F.; Carof, A.; Breuer, M.; Blumberger, J. Cysteine Linkages Accelerate Electron Flow through Tetra-Heme Protein STC. *J. Am. Chem. Soc.* **2017**, *139*, 17237–17240.

(21) Jiang, X.; van Wonderen, J. H.; Butt, J. N.; Edwards, M. J.; Clarke, T. A.; Blumberger, J. Which Multi-Heme Protein Complex Transfers Electron More Efficiently? Comparing MtrCAB from Shewanella with OmcS from Geobacter. *J. Phys. Chem. Lett.* **2020**, *11*, 9421–9425.

(22) van Wonderen, J. H.; Li, D.; Piper, S. E. H.; Lau, C. Y.; Jenner, L. P.; Hall, C. R.; Clarke, T. A.; Watmough, N. J.; Butt, J. N. Photosensitised Multiheme Cytochromes as Light-Driven Molecular Wires and Resistors. *ChemBioChem* **2018**, *19*, 2206–2215.

(23) van Wonderen, J. H.; Hall, C. R.; Jiang, X.; Adamczyk, K.; Carof, A.; Heisler, I.; Piper, S. E. H.; Clarke, T. A.; Watmough, N. J.; Sazanovich, I. V. et al. Ultrafast Light-

Driven Electron Transfer in a Ru(II)tris(bipyridine)-Labeled Multiheme Cytochrome. *J. Am. Chem. Soc.* **2019**, *141*, 15190–15200.

(24) van Wonderen, J.; Adamczyk, K.; Wu, X.; Jiang, X.; Piper, S. E. H.; Hall, C. R.; Edwards, M. J.; Clarke, T. A.; Zhang, H.; Jeuken, L. J. C. et al. Nanosecond Heme-to-Heme Electron Transfer Rates in a Multiheme Cytochrome Nanowire Reported by a Spectrally Unique His/Met-Ligated Heme. *Proc. Nat. Acad. Sci.* **2021**, *118*, e2107939118.

(25) Lienemann, M. Molecular Mechanism of Electron Transfer Employed by Native Proteins and Biological-Inorganic Hybrid Systems. *Comput. Struct. Biotech. J.* **2021**, *19*, 206–213.

(26) Jiang, X.; Burger, B.; Gajdos, F.; Bortolotti, C.; Futera, Z.; Breuer, M.; Blumberger, J. Kinetics of Trifurcated Electron Flow in the Decaheme Bacterial Proteins MtrC and MtrF. *Proc. Nat. Acad. Sci.* **2019**, *116*, 3425–3430.

(27) Cahen, D.; Pecht, I.; Sheves, M. What Can We Learn from Protein-Based Electron Transport Junctions? *J. Phys. Chem. Lett.* **2021**, *12*, 11598–11603.

(28) Giannini, S.; Blumberger, J. Charge Transport in Organic Semiconductors: The Perspective from Nonadiabatic Molecular Dynamics. *Acc. Chem. Res.* **2022**, *55*, 819–830.

(29) Papp, E.; Jelenfi, D. P.; Veszeli, M. T.; Vattay, G. A Landauer Formula for Bioelectronic Applications. *Biomol.* **2019**, *9*, 599.

(30) Wang, K.-C.; Grassi, R.; Chu, Y.; Sureshbabu, S. H.; Geng, J.; Sarangapani, P.; Guo, X.; Townsend, M.; Kubis, T. Introduction of Multi-Particle Buttiker Probes - Bridging the Gap between Drift Diffusion and Quantum Transport. *J. Appl. Phys.* **2020**, *128*, 14302.

(31) Futera, Z.; Ide, I.; Kayser, B.; Garg, K.; Jiang, X.; van Wonderen, J. H.; Butt, J. N.; Ishii, H.; Pecht, I.; Sheves, M. et al. Coherent Electron Transport across a 3 nm Bio-electronic Junction Made of Multi-Heme Proteins. *J. Phys. Chem. Lett.* **2020**, *11*, 9766–9774.

(32) Amdursky, N.; Sepunaru, L.; Raichlin, S.; Pecht, I.; Sheves, M.; Cahen, D. Electron Transfer Proteins as Electronic Conductors: Significance of the Metal and Its Binding Site in the Blue Cu Protein, Azurin. *Adv. Sci.* **2015**, *2*, 1400026.

(33) Agam, Y.; Nandi, R.; Kaushansky, A.; Peskin, U.; Amdursky, N. The Porphyrin Ring Rather than the Metal Ion Dictates Long-Range Electron Transport across Proteins Suggesting Coherence-Assisted Mechanism. *Proc. Nat. Acad. Sci.* **2020**, *117*, 32260–32266.

(34) El-Naggar, M. Y.; Wanger, G.; Leung, K. M.; Yuzvinsky, T. D.; Southam, G.; Yang, J.; Lau, W. M.; Nealson, K. H.; Gorby, Y. A. Electrical Transport along Bacterial Nanowires from Shewanella oneidensis MR-1. *Proc. Nat. Acad. Sci.* **2010**, *107*, 18127–18131.

(35) Giese, B.; Amaudrut, J.; Kohler, A.-K.; Spormann, M.; Wessely, S. Direct Observation of Hole Transfer through DNA by Hopping Between Adenine Bases and by Tunneling. *Nature* **2001**, *412*, 318–320.

(36) Van Nguyen, Q.; Frisbie, C. D. Hopping Conductance in Molecular Wires Exhibits a Large Heavy-Atom KKinetic Isotope Effects. *J. Am. Chem. Soc.* **2021**, *143*, 2638–2643.

(37) Iori, F.; Di Felice, R.; Molinari, E.; Corni, S. GoIP: An Atomistic Force-Field to Describe the Interaction of Proteins With Au(111) Surfaces in Water. *J. Comput. Chem.* **2009**, *30*, 1465–1476.

(38) Wright, L. B.; Rodger, P. M.; Corni, S.; Walsh, T. R. GoIP-CHARMM: First-Principles

Based Force Fields for the Interaction of Proteins with Au(111) and Au(100). *J. Chem. Theory Comput.* **2013**, *9*, 1616–1630.

(39) Futera, Z.; Blumberger, J. Adsorption of Amino Acids on Gold: Assessing the Accuracy of the GolP-CHARMM Force Field and Parametrization of Au-S Bonds. *J. Chem. Theory Comput.* **2019**, *15*, 613–624.

(40) Thompson, A. P.; Plimpton, S. J.; Mattson, W. General Formulation of Pressure and Stress Tensor for Arbitrary Many-Body Interaction Potentials under Periodic Boundary Conditions. *J. Chem. Phys.* **2009**, *131*, 154107.

(41) Ollila, O. H. S.; Risselada, H. J.; Louhivuori, M.; Lindahl, E.; Vattulainen, I.; Marrink, S. J. 3D Pressure Field in Lipipd Membranes and Membrane-Protein Complexes. *Phys. Rev. Lett.* **2009**, *102*, 78101.

(42) Perdew, J. P.; Burke, K.; Ernzerhof, M. Generalized Gradient Approximation Made Simple. *Phys. Rev. Lett.* **1996**, *77*, 3865–3868.

(43) Goedecker, S.; Teter, M.; Hutter, J. Separable Dual-Space Gaussian Pseudopotential. *Phys. Rev. B* **1996**, *54*, 1703–1710.

(44) Hutter, J.; Iannuzzi, M.; Schiffmann, F.; VandeVondele, J. CP2K: Atomistic Simulations of Condensed Matter Systems. *WIREs Comput. Mol. Sci.* **2014**, *4*, 15–25.

(45) Futera, Z.; Blumberger, J. Electronic Couplings for Charge Transfer across Molecule/Metal and Molecule/Semiconductor Interfaces: Performance of the Projector Operator-Based Diabatization Approach. *J. Phys. Chem. C* **2017**, *121*, 19677–19689.

(46) Neaton, J. B.; Hybertsen, M. S.; Louie, S. G. Renormalization of Molecular Electronic Levels at Metal-Molecule Interfaces. *Phys. Rev. Lett.* **2006**, *97*, 216405.

(47) Egger, D. A.; Liu, Z.-F.; Neaton, J. B.; Kronik, L. Reliable Energy Level Alignment

at Physisorbed Molecule-Metal INterfaces from Density Functional Theory. *Nano Lett.* **2015**, *15*, 2448–2455.

(48) Gillet, N.; Berstis, L.; Wu, X.; Gajdos, F.; Heck, A.; de la Lande, A.; Blumberger, J.; Elstner, M. Electronic Coupling Calculations for Bridge-Mediated Charge Transfer Using Constrained Density Functional Theory (CDFT) and Effective Hamiltonian Approaches at the Density Functional Theory (DFT) and Fragment-Orbital Density Functional Tight Binding (FODFTB) Level. *J. Chem. Theory Comput.* **2016**, *12*, 4793–4805.

(49) Ziogos, O. G.; Kubas, A.; Futera, Z.; Xie, W.; Elstner, M.; Blumberger, J. HAB79: A New Molecular Dataset for Benchmarking DFT and DFTB Electronic Couplings Against High-Level Ab Initio Calculations. *J. Chem. Phys.* **2021**, *155*, 234115.

(50) Byun, H. S.; Pirbadian, S.; Nakano, A.; Shi, L.; El-Naggar, M. Y. Kinetic Monte Carlo Simulations and Molecular Conductance Measurements of the Bacterial Decaheme Cytochrome MtrF. *ChemElectroChem* **2014**, *1*, 1932–1939.

(51) Wigginton, N. S.; Rosso, K. M.; Hochella, M. F. J. Mechanism of Electron Transifer in Two Decaheme Cytochromes from a Metal-Reducing Bacterium. *J. Phys. Chem. B* **2007**, *111*, 12857–12864.

(52) Baratz, A.; Galperin, M.; Baer, R. Gate-Induced Intramolecular Charge Transfer in a Tunnel Junction: A Nonequilibrium Analysis. *J. Phys. Chem. C* **2013**, *117*, 10257–10263.

(53) Yates, M. D.; Golden, J. P.; Roy, J.; Strycharz-Glaven, S. M.; Tsoi, S.; Erickson, J. S.; El-Naggar, M. Y.; Barton, S. C.; Tender, L. M. Thermally Activated Long Range Electron Transport in Living Biofilms. *Phys. Chem. Chem. Phys.* **2015**, *17*, 32564–32570.

(54) Huang, J.; Zarzycki, J.; Gunner, M. R.; Parson, W. W.; Kern, J. F.; Yano, J.;

Ducat, D. C.; Kramer, D. M. Mesoscopic to Macroscopic Electron Transfer by Hopping in a Crystal Network of Cytochromes. *J. Am. Chem. Soc.* **2020**, *142*, 10459–10467.

(55) Simmons, J. G. Generalized Formula for the Electric Tunnel Effect between Similar Electrodes Separated by a Thin Insulating Film. *J. Appl. Phys.* **1963**, *34*, 1793–1803.

(56) Zhang, Y.; Liu, C.; Balaeff, A.; Skourtis, S. S.; Beratan, D. N. Biological Charge Transfer via Flickering Resonance. *Proc. Nat. Acad. Sci.* **2014**, *111*, 10049–10054.